Nano Energy 73 (2020) 104785

Contents lists available at ScienceDirect

Nano Energy

journal homepage: http://www.elsevier.com/locate/nanoen

# Cephalopod-inspired versatile design based on plasmonic $VO_2$ nanoparticle for energy-efficient mechano-thermochromic windows

Yujie Ke [a,**,1], Qiuting Zhang [b,c,1], Tao Wang [d], Shancheng Wang [a], Na Li [a,e], Gaojian Lin [f], Xinghai Liu [g], Zhendong Dai [h], Jing Yan [b], Jie Yin [c], Shlomo Magdassi [i], Dongyuan Zhao [j], Yi Long [a,k,l,*]

[a] School of Materials Science and Engineering, Nanyang Technological University, Singapore, 639798, Singapore
[b] Department of Molecular, Cellular and Developmental Biology, Yale University, New Haven, 06511, Connecticut, USA
[c] Department of Mechanical and Aerospace Engineering, North Carolina State University, Raleigh, NC, 27695, USA
[d] Institute of Functional Nano & Soft Materials (FUNSOM), Jiangsu Key Laboratory for Carbon-Based Functional Materials & Devices, Collaborative Innovation Center of Suzhou Nano Science and Technology, Soochow University, Suzhou, 215123, Jiangsu, China
[e] College of Chemistry and Chemical Engineering, Northeast Petroleum University, Daqing, 163000, Heilongjiang, China
[f] School of Mechatronical Engineering, Beijing Institute of Technology, Beijing, 100081, China
[g] School of Printing and Packaging, Wuhan University, Wuhan, 430072, China
[h] Institute of Bio-Inspired Structure and Surface Engineering, Nanjing University of Aeronautics and Astronautics, Nanjing, 210016, China
[i] Casali Center for Applied Chemistry Institute of Chemistry, The Center for Nanoscience and Nanotechnology, The Hebrew University of Jerusalem, Jerusalem, 9190401, Israel
[j] Department of Chemistry, Shanghai Key Laboratory of Molecular Catalysis and Innovative Materials, Laboratory of Advanced Materials, iChEM (Collaborative Innovation Center of Chemistry for Energy Materials), Fudan University, Shanghai, 200433, China
[k] Singapore-HUJ Alliance for Research and Enterprise (SHARE), Campus for Research Excellence and Technological Enterprise (CREATE), Singapore, 138602, Singapore
[l] Sino-Singapore International Joint Research Institute (SSIJRI), Guangzhou, 510000, China

ARTICLE INFO

*Keywords:*
Bio-inspired
Localized surface plasmon resonance
Wrinkle
Smart window
Mechanochromic
Solar energy modulation

ABSTRACT

Privacy and energy-saving are key functionalities for next-generation smart windows, while to achieve them independently on a window is challenging. Inspired by the cephalopod skin, we have developed a versatile thermo- and mechano-chromic design to overcome such challenge and reveal the mechanism via both experiments and simulations. The design is facile with good scalability, consisted of well-dispersed vanadium dioxide ($VO_2$) nanoparticles (NPs) with temperature-dependent localized surface plasmon resonance (LSPR) in transparent elastomers with dynamic micro wrinkles. While maintaining a fixed solar energy modulation of ($\Delta T_{sol}$), the design can dynamically control visible transmittance ($T_{vib}$) from 60% to 17%, adding a new dimension to $VO_2$-based smart windows. We prove that the optical modulation relies on the microtexture-induced broadband diffraction and the plasmon-enhanced near-infrared absorbance of $VO_2$ NPs. We further present a series of modified designs towards additional functionalities. This work opens an avenue for independent dual-mode windows and it may inspire development from fundamental material, optic, and mechanical science to energy-related applications.

## 1. Introduction

The smart window technology, referring to on-demand windows that dynamically modulate their transmittances, has been recognized as a promising direction for next-generation windows [1–3]. The strong driving force from both industry and academics leads to a rapid development of the technology in the past few years, expending its applications in extensive areas, such as architectures, aircraft, and automobile [1]. These applications can be divided into two main functionalities [4–6]: 1) energy-saving windows to dynamically control the indoor solar

* Corresponding author. School of Materials Science and Engineering, Nanyang Technological University, Singapore, 639798, Singapore.
** Corresponding author.
*E-mail addresses:* yujie.ke@ntu.edu.sg (Y. Ke), longyi@ntu.edu.sg (Y. Long).
[1] These authors contribute equally.

https://doi.org/10.1016/j.nanoen.2020.104785
Received 26 February 2020; Received in revised form 20 March 2020; Accepted 30 March 2020
Available online 21 April 2020

modulation, and 2) on-demand privacy windows to selectively block the view image.

So far, a number of methods can successfully achieve these functionalities, including the electro- [7–10], mechano- [11,12], and thermo-chromics [13–15], while to separate these two functionalities on a window is challenging since both strongly rely on the transmittance change. For example, the most investigated type of electrochromic window based on the redox reaction of metal oxide [8,16], the dynamic ion insertion [17,18], or the reversible electrodeposition [19], modulates the transmittance by tuning the absorbance; in this case, changes in transmitted optical energy are inevitable when visible view changes.

The dynamic color-change of cephalopod skin represents an exciting source of inspiration for the development of diverse optical modulation systems for infrared-reflection [20], thermoregulator [21], display [22], camouflage [23], and so on [24]. Cephalopods can actively control their appearance by altering the sophisticated architecture of the skin (Fig. 1a) [20,25]. As a functional cell in skin, the iridocytes possess alternating arrangements of protein layers and extracellular space, offering refractive index and geometrical difference as Bragg stacks (Fig. 1a). The geometry is actively controlled by the cells for selective light reflection, thus to dynamically change the skin color (Fig. 1a).

Inspired by the cephalopod, hereby we present a versatile thermo-mechano-chromics design to fulfil the energy-saving and privacy functionalities independently in one window. The design consists consisting of thermochromic nanoparticles (NPs) within mechanochromic bilayer structures. It is facile, highly flexible for modification, and easy-processible for large-scale. Using both experimental and simulation approaches, we reveal that the energy-saving mode is achieved by the thermochromic NPs due to their temperature-dependent near-infrared (NIR) absorbance of vanadium dioxide ($VO_2$) based on its active localized surface plasmon resonance (LSPR). The privacy mode is attributed to the controllable broadband diffraction via the strain-induced dynamically tunable surface structures (dynamic wrinkles). Both the spectrum and demonstrations indicate that these two modes work independently. The design is highly flexible as it can, for example, control patterning, change the top layer or NPs, modify the surface wettability, make double-side design for performance enhancement, and fabricate to inverse mechanochromic design.

## 2. Experimental

### 2.1. Preparation of the PVA-based thermo-mechanochromic films

In general, the films were prepared by coating the pre-fabricated $VO_2$-PDMS elastomers with the top PVA layers. Unless specified, the cephalopod-Inspired structures were formed by pre-stretching the prepared films to 175% length and released to its original 100% length.

The $VO_2$-PDMS elastomers were prepared by curing the base and curing agent of PDMS (Sylgard 184, Dow Corning) with the mixture of $VO_2$ NPs (Jincheng China). In detail, 18-mg $VO_2$, 1.2-g PDMS curing agent, 12-g PDMS base, and 54-ml hexane (Aik Moh, Singapore) were mixed in a glass bottle, followed by an overnight magnetic stir and 4-h ultrasonic process to have the NPs well-dispersed. The hexane was added to assist the dispersion of $VO_2$ and slow down the curing process of PDMS at room temperature, and it would be removed later. After 3-day isolation process, 10.5 ml of supernatant was transferred to a plastic petri dish with a diameter of 5.5 mm. The hexane is removed by ~6-h evaporation at room temperature in a fume hood. Then, the stiff mixture is curing in an oven under 60 °C for ~4 h. The preparation method of elastomers based on W-doped $VO_2$ (Jincheng China) is the same as it of the $VO_2$-PDMS elastomers.

The coating methods vary from different top layers. The PVA (Sigma Aldrich) top layer was prepared by drop-casting 2.4-ml its aqueous solution (5.0 wt%) onto the O-plasma treated $VO_2$-PDMS elastomers. The PVA and HPC solutions were prepared in a 90-$^{o}$C water bath until there were fully dissolved. The O-plasma treatment was conducted with an RF power of 100 W for 10 s using a plasma cleaner (Convance-2MPR, Femto Science). The treatment process is to make the elastomer surface hydrophilic to be suitable for drop-casting of aqueous solution. Double-side PVA-coated samples were prepared by the drop-casting process twice on both sides of the $VO_2$-PDMS elastomers.

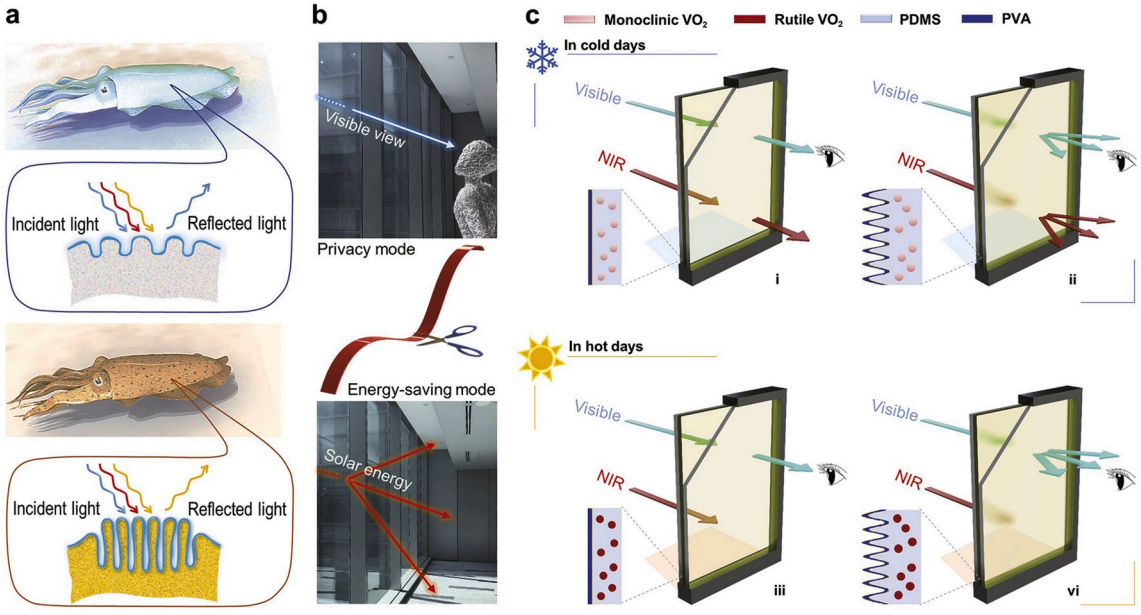


**Fig. 1.** Inspiration from cephalopod skin and rationale for the film design. (a) Schematic of how a cephalopod changes appearance change by tuning its Bragg stack architecture of the skin to selectively reflect incident light. (b) Illustration of the rationale to untangle the privacy and energy-saving modes through distinguishing the acceptors, which are human eyes for the privacy mode and the entire room for the energy-saving mode, respectively. (c) Schematic of the film consisted of well-dispersed $VO_2$ (M/R) NPs in the PVA-PDMS bilayer structure, and its four representative states of the design to meet the different window modes: (c i) normal, (c ii) privacy, (c iii) energy-saving, and (c vi) simultaneous energy-saving and privacy mode without interferences.

### 2.2. Preparation of the films beyond PVA-based

The same elastomers preparation method is applied to all samples, while the coating methods vary according to the different top layers, which are detailed as follows.

Highly hydrophilic samples were prepared via an O-plasma treatment of 100 W for 20 s to the PVA surface of PVA-based thermo-mechanochromic films. Hydrophobic samples were prepared by coating a thin layer of OTS (Sigma Aldrich) solution onto the PVA surface of PVA-based thermo-mechanochromic films, following by 50 °C in oven for 2 h to remove the solvent. The OTS was dissolved in 1.0 vol% in hexane. The HPC (Sigma Aldrich) layer was prepared using the same method as the PVA-based films. These films based on organic coating were pre-stretched to 175% of its original length and released for further use, while inorganic layers were coated at either stretch or release state without further pre-stretch process. The Pt-layer samples were prepared by coating the pre-stretched $VO_2$-PDMS elastomers (75% elongated) with Pt thin film using a sputter coating system (JEC3000-FC, JEOL Asia) under the condition of 30 mA and 50 s. The inverse mechano-chromic design of Pt-layer samples was prepared via the same process but using the $VO_2$-PDMS elastomers without pre-strain that is the release state. The $SiO_x$-layer samples were prepared through the O-plasma treatment onto the release state of $VO_2$-PDMS elastomers under 100 W for 60 s.

### 2.3. Mechanical simulation

We use the commercial finite element software ABAQUS to simulate the wrinkling formation process in the PVA/PDMS with a strain mismatch. In the finite element model as shown in Fig. S25, we model the PVA/PDMS as a bilayer system. In the undeformed state, the buckling eigenmode is introduced as an imperfection to simulate the following post-buckling process. The thickness of the PVA thin film is 1.2 μm with Young's modulus $E_f = 175$ MPa. The hyperelastic Neo-Hookean model is employed to model the PDMS substrate with inputting tested data. Fine mesh is applied to both the thin film and top part of the substrate with a total number of elements of 127,394 in the model system. The element type for both film and substrate is CPE4R.

### 2.4. Optical simulation

To simulate the far-field spectra and the near-field distributions, three-dimensional finite difference time domain (3D-FDTD) simulations were performed using Lumerical FDTD Solutions. In the simulation, a total-field scattered-field (TFSF) source was chosen; a simulation region of 500 nm × 500 nm × 500 nm was used, and perfectly matched layers were defined as boundary conditions. A fine mesh size of 0.5 nm × 0.5 nm × 0.5 nm was used. For the far-field spectra in Fig. 4d, the scattering and absorption spectra of a single $VO_2$ NP (M/R) with a diameter of 100 nm in PDMS medium was simulated. For the near-field responses shown in Fig. 4c, the electric field distribution of the single NP (M/R) at the resonance wavelength was simulated. The optical dielectric constant of $VO_2$ and PDMS are taken from previous reports [26].

The TMM calculation for Fig. 4e involves 3 layers: the top air layer, the bottom air layer, and the $VO_2$ NP decorated PDMS layer (of 5 μm thick) with the effective optical dielectrics $\varepsilon_{\text{eff}}$ defined as follows:

$$\varepsilon_{eff} = \varepsilon_{eff}\frac{1+\frac{2}{3}f\alpha_{VO_2}}{1-\frac{1}{3}f\alpha_{VO_2}} \tag{1}$$

$$\alpha_{VO_2} = \frac{\varepsilon_{VO_2}-\varepsilon_{PDMS}}{\varepsilon_{PDMS}+\frac{\varepsilon_{VO_2}-\varepsilon_{PDMS}}{3}} \tag{2}$$

Where $\varepsilon_{\text{PDMS}}$, $\varepsilon_{\text{VO2}}$ as the optical dielectrics of PDMS and $VO_2$, $f$ as the filling factor, and $\alpha_{\text{vo2}}$ as the polarizability of the $VO_2$ NP. The characteristic matrix of the system is:

$$\left[\cos(kd) - i\sin(kd)/_k - ik\sin(kd)\cos(kd)\right] \tag{3}$$

where $k$ is the wave number of light in the $VO_2$ NP decorated PDMS layer and $d$ is the thickness of the $VO_2$ NP decorated PDMS layer.

### 2.5. Characterization

The crystal phase was identified in a two-theta mode (a fixed incident angle of 1.0°) at room temperature by a thin-film glancing angle XRD (XRD-6000, Shimadzu) with Cu Kα X-ray. The temperature-dependent crystal phases were conducted at temperatures from 25-90 °C during a heating process.in a two-theta mode (a fixed incident angle of 1.0°) by the XRD (D8 Advance, Bruker) with Cu Kα X-ray. Crystal lattice and structure were characterized using a TEM (JEM2010, JEOL) at an accelerating voltage of 200 kV. Crystal morphology and size were identified using a FESEM (6340F, JEOL) at an accelerating voltage of 5 kV. For the privacy mode test, the spectra were measured by the UV-vis-NIR spectrophotometry (Cary 5000, Agilent) using the single point detector. For the energy-saving mode test, the spectra were measured by the UV-vis-NIR spectrophotometry (Lambda 950, Perkin Elmer), equipment with a 150 mm integrating spheres for signal collection. The spectrophotometries were integrated with an accessory containing a customized heating and cooling stage and a digital controller (PE120, Linkam) for temperature-dependent measurement. Films were pre-stretched to certain length and fixed to the sample holder for strain-dependent spectrum measurement. Surface topology is measured using an optical surface profiler (Smart proof 5, Zeiss). Wettability is identified using a contact angle test system (OCA 15 Pro, DataPhysics). Digital photographs were taken using the phone camera (iPhone 6 plus, Apple). The diffraction tests were conducted using the lasers of 650, 450, and 532 nm for blue, green, and red, respectively. The thermal radiation test was conducted using a customized design with a source of spotlight (Spot R80, 100 W, General Electric). Calculation methods for visible transmittance ($T_{\text{vib}}$, 380–780 nm), integrated luminous transmittance ($T_{\text{lum}}$, 380–780 nm) and solar energy modulation ($\Delta T_{\text{sol}}$, 250–2500 nm) are indicated in Note S1.

## 3. Results and discussion

### 3.1. Design rationale

In this work, we aim to untangle the privacy and energy-saving modes in one window (Fig. 1b). Despite the fact that both energy-saving and privacy functionalities rely on the light modulation, they are fundamentally different regarding 1) the target spectrum and 2) the acceptors. Firstly, the energy-saving mode concerns the full solar spectrum ranging from ultraviolet, visible, to near-infrared (UV-vis-NIR), while the privacy mode concerns only the visible light (Fig. 1b). Secondly and more importantly, the energy-saving and privacy windows have different responses to light transmission by a room and human eyes, respectively (Fig. 1b). That means the acceptor for energy-saving windows is an area (rooms), in contrast to a point (human eyes) for privacy windows (Fig. 1b). This difference is important, for example, considering the light scattering effect. The incident light can be redirected, leading to a much lower transmission to the point acceptor (human eyes), but likely inducing relatively less change of integrated intensity to the area acceptor (room). To our knowledge, the distinction between these two modes from this fundamental perspective has not been proposed yet in literature, which serves as the foundation for the thermo-mechano-chromic design presented as follows (Fig. 1b).

The design is constructed of two parts: a mechnochromic structure with dynamic diffraction for privacy mode and a themrochromic material with tunable NIR absorbance for energy-saving mode. As an example (Fig. 2c), a bilayer structure is prepared with thin polyvinyl

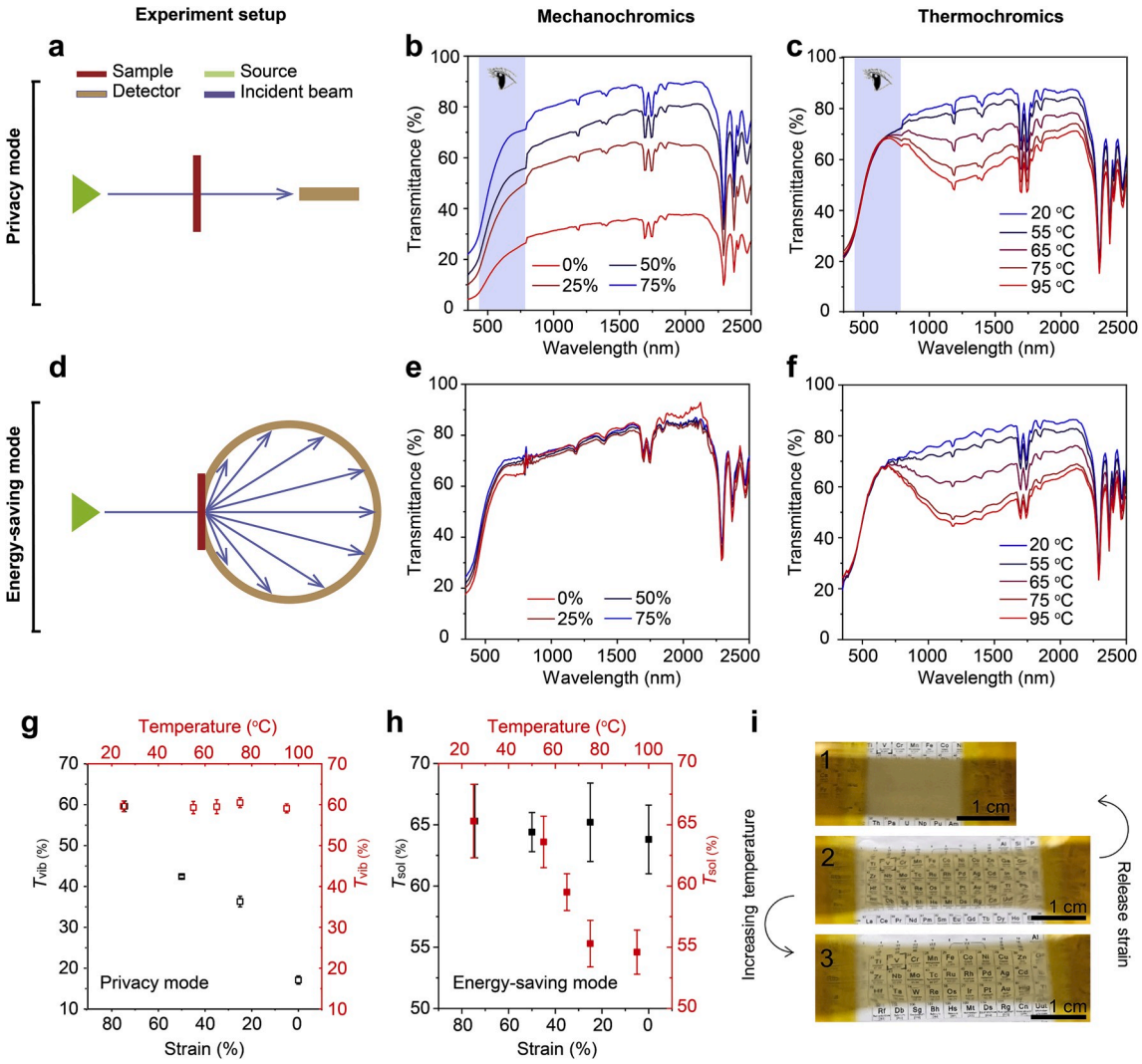


**Fig. 2.** Dynamic and independent optical modulation. (a–c) Results of the film for privacy mode. (a) Illustration of the spectrum measurement setup to mimic the privacy mode and recorded spectra of the film under (b) strain and (c) thermal response. The visible spectrum is indicated as light blue. (d–f) Results of the film for energy-saving mode. (d) Illustration of the spectrum measurement setup to mimic the energy-saving mode and recorded spectra of the film under (e) strain and (f) thermal response. (g–h) Analysis of the performance of (g) privacy ($T_{vib}$) and (h) energy-saving ($T_{sol}$) modes. The black and red points indicate the results under different strain and temperature, respectively. (i) Photographs of the film and its appearance under (i 1) no strain, (i 2) strain of 75% and (i 3) elevated temperature of 95 °C.

alcohol (PVA) top layer and a polydimethylsiloxane (PDMS) elastomer base containing well-dispersed $VO_2$ NPs. PDMS and PVA are used due to their relatively high transparency in the UV-vis-NIR spectrum (Fig. S1). The top PVA thin layer is measured to be ~1.2 μm (Fig. S2). The volume of PDMS and concentration of $VO_2$ are fixed and described in the preparation method. The $VO_2$ NPs have an average diameter of ~60 nm with a narrow size distribution (Fig. S3), and no other phase is detectable besides monoclinic (M) $VO_2$ based on room-temperature X-ray diffraction (XRD) analysis (Fig. S4). The morphology, size and crystal structure of the applied $VO_2$ NPs are further identified using the transmission electron microscopy (TEM) (Fig. S5). Moreover the film can be produced on a large scale, for example more than 10 cm in diameter (Fig. S6).

The smart window based on such films can present an active view control and adaptive energy-saving functionalities simultaneously and independently (Fig. 1c). In cold days, solar energy includes NIR and visible light that can pass through the window to indoor, and the view is controlled by redirecting the visible light to reduce its intensity received by human eyes (Fig. 1c i and ii). On hot days, however, the NIR energy is adaptively blocked to reduce indoor solar irradiation, and the unblocked visible light is controlled in the same way as in cold days for privacy mode(Fig. 1c iii and vi). For the functional film, the thermochromic energy-saving mode relies on the temperature-dependent reversible phase transition between $VO_2$ M (Fig. 1c i and ii) and rutile (R) (Fig. 1c iii and vi) phases, while the mechanochromic privacy mode is achieved by stretching or releasing the film, leading to a reversible switches between flat surface (Fig. 1c i and iii) and wrinkled texture (Fig. 1c ii and vi). Since the two modes are fundamentally different in both stimulus methods (strain and temperature) and the resulting optical modulation (diffraction and absorbance), they can work simultaneously and independently.

### 3.2. Dynamic and independent optical modulation

To explore if the film can achieve the proposed functionalities independently, its transmittance spectra were measured using a point detector to mimic human eyes in the privacy mode (Fig. 2a–c) and an enclosed surface detector (integrating sphere) to mimic a room in the energy-saving mode (Fig. 2d–f).

For the privacy mimic, the setup for point detector measurement is

illustrated in Fig. 2a, where only the beam through the film in alignment with the incident direction is recorded by the detector. We found that the visible transmittance significantly decreases when releasing the strain from 75% to 0% (Fig. 2b), while no significant change in the visible spectrum is observed when varying the temperature from 25 to 95 °C (Fig. 2c). Though the transmittance changes in UV and NIR ranges (area beyond blue in Fig. 2b,c) are significant, they are not detectable by human eyes. The result demonstrated that in the film, the strain works independently from the temperature to control visible light transmitted in alignment with the incident direction.

To mimic the energy-saving mode, we build a setup based on an enclosed surface detector to collect the entire light transmission passing through the film (Fig. 2d). No significant change was detected in UV-vis-NIR transmittance under different strains ranging from 0% to 75% (Fig. 2e), suggesting that variable strain makes a negligible contribution to optical energy modulation. However, a significant decrease in NIR spectrum is observed, accompanied with nearly the same intensity in UV spectrum when elevating the temperature (Fig. 2f). Thus, the temperature stimulus can dynamically control the energy carried by NIR, while keeping visible transparency constant. The result indicates that the temperature stimulus works independently from strains to modulate the optical energy of invisible NIR favourably.

To further assess the modulations, we take into account the spectral sensitivity of human visual perception (Fig. S7) for the point-detector measurement (privacy mode) and the solar energy distribution (Fig. S8) for the result of enclosed surface detector (energy-saving mode), and calculate visible transmittance ($T_{vib}$) and transmitted solar energy ($T_{sol}$) for performance assessment (Note S1). As to the point detector, the $T_{vib}$ decreases under a releasing strain from ~60% to ~17%, while it remains constant under increasing temperature (Fig. 2g). However, for the surface detector, the $T_{sol}$ drops from ~65.5% at 25 °C to ~54.0% at 95 °C, and maintains relatively unchanged at ~65% under different strains (Fig. 2h). This analysis again suggests that $T_{vib}$ and $T_{sol}$ are solely controlled by the strain and temperature, respectively. Current smart windows based on pure $VO_2$ cannot modulate the passing visible view under a fixed $\Delta T_{sol}$ (Fig. S9) [2,4]. While maintaining a $\Delta T_{sol}$ of ~11.5%, the film is able to change its $T_{vib}$ of ~60% as transparent state to $T_{vib}$ of ~17% as privacy state, adding a new dimension to the design of $VO_2$-based smart windows (Fig. S9) [2,4]. It is worthwhile mentioning that its mechanochromic and thermochromic performances are different from each other in the sense that the former is inconsistent while the latter one remains constant under measurements using different detectors (Fig. S10). The performance of visible modulation is further confirmed by photo images of the film under temperature and strain stimuli (Fig. 2i). The background periodic table can be viewed clearly through the room-temperature stretched state (Fig. 2i 2) but is totally blocked when it is in the released state (Fig. 2i 1), while there is no observable transparency change when elevating its temperature to 95 °C (Fig. 2i 3). These two dynamic processes are also recorded in Video S1 and S2, which are consistent with the corresponding spectrum and photo image results.

Supplementary video related to this article can be found at https://doi.org/10.1016/j.nanoen.2020.104785

### 3.3. Mechanism of mechanochromics

Tunable surface topography is measured on the PVA side of the bilayer structure and the wrinkle structures are observed to gradually disappear under an increasing strain from 0% to 75% (Fig. 3a). The evolution is further confirmed by the top-view optical microscopy images, in which the paralleled patterns disappear gradually from 0% to 75% (Fig. S11). The geometrical dimensions of the periodic wrinkles are characterized by 1/2 peak height (amplitude) and the periodicity (wavelength), respectively. Here, in the 1.2-μm PVA sample, the amplitude and wavelength are identified respectively to be ~1.3 and ~18 μm at 0% applied strain (a fully released state) (Fig. 3a). Upon stretching, the wrinkles gradually disappear to a flatten surface due to the decrease of strain mismatch between the PVA layer and PDMS substrate. The structure evolution during stretching process is also confirmed by simulation using finite element method (FEM), where an

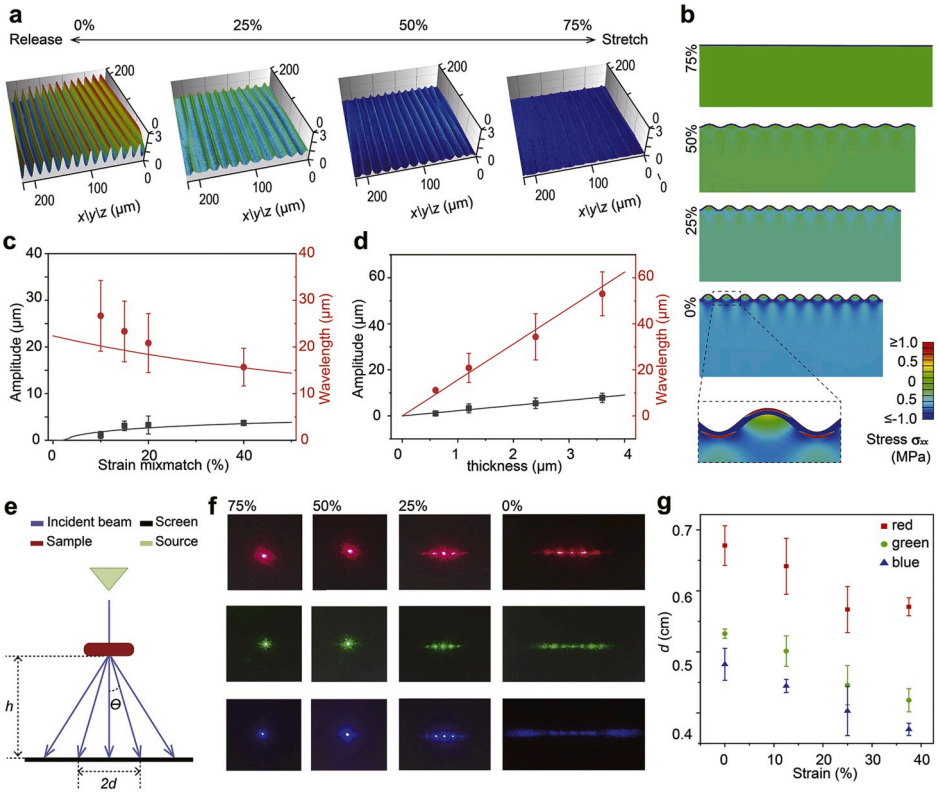


**Fig. 3.** Mechanochromics based on wrinkle-induced diffraction. (a) Experimental surface topology of the film under applied strains from 0% to 75%. (b) FEM-simulated structure and the strain distribution contour under applied strains from 0% to 75%. (c–d) Amplitude and wavelength of the wrinkle structures under different (c) thickness of PVA layer and (d) strain mismatch. Experiment and theoretical results are indicated as the points and lines, respectively. (e–g) Diffraction measurement and the results. (e) Schematic of the experimental setup for the diffraction measurement. (f) Recorded diffraction patterns using the laser with wavelength of 650, 450, and 532 nm under different applied strains (0%–75%). (g) Experimental and theoretical analysis of the effect of applied strain and incident light wavelength to the 1st order diffraction angle.

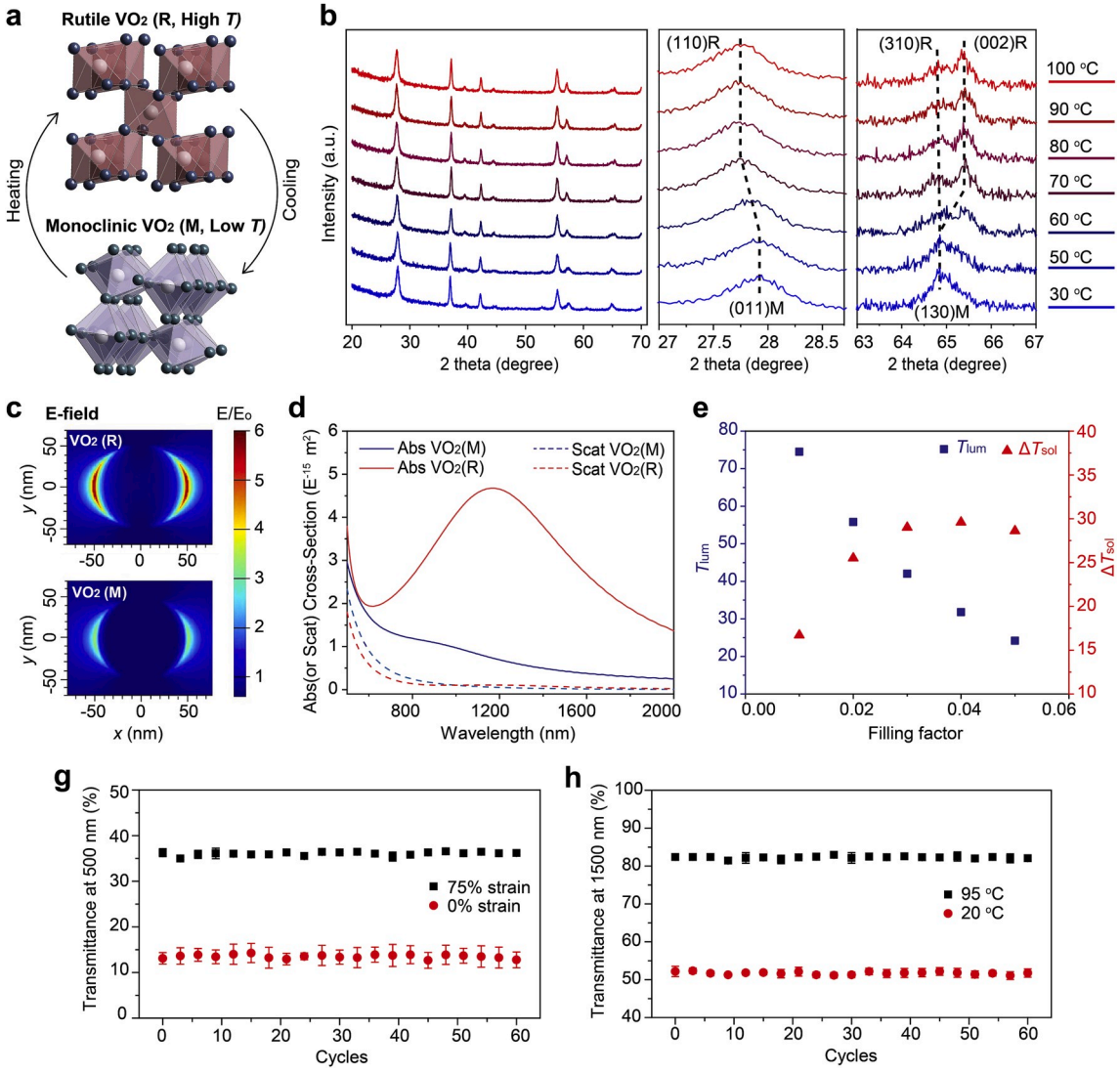


**Fig. 4.** Thermochromics based on active plasmon and durability. (a) Illustration of the reversible crystal phase transition of $VO_2$ between the high-temperature R phase and the low-temperature M phase. (b) XRD analysis of the $VO_2$ (R/M) at temperature from 25 to 90 °C. Figures on the right are the magnified XRD results at 2-theta degree of ~27.0–28.5° and ~63.0–66.5°. Blue lines are the trend lines to indicate the peak shift and split. (c) E-field ($x$–$y$) of a $VO_2$(R/M) NP in PDMS matrix. (d) Calculated absorbance and scattering spectra of a $VO_2$ (R/M) NP in PDMS matrix. (e) Calculated $T_{lum}$ and $\Delta T_{sol}$ of $VO_2$ in PDMS matrix in the filling factor varying from 0.01 to 0.05. (f–g) Cycling tests of the film under alternate (f) applied strain (0–75%) and (g) temperature (25–95 °C).

increasing applied strain by stretching the film leads to the gradual disappearance of the wrinkles (Fig. 3b). It is also revealed that local strain maxima preferentially accumulate in zones with relatively larger curvatures, such as peaks or valleys of the winkle structures (Magnified strain contour in Fig. 3b).

Wrinkling structures on the PVA side are generated during the sample preparation process by pre-stretching the PVA-PDMS bilayer. After releasing, strain mismatch between the two different layers gives rise to a spontaneous periodic wrinkling structure. These wrinkling structures can be reversibly stretched back to a flattened surface. The produced wrinkling structures are strongly related to the pre-strain during preparation process (Fig. 3c) and the thickness of PVA layer (Fig. 3d). The pre-strain during film preparation determines the maximum PVA-PDMS strain mismatch in the film (Fig. S12). When the mismatched strain increases from 10% to 40%, the amplitude rises from ~1 to ~4 μm, while the wavelength is observed to decrease from ~27 to 15 μm (Fig. 3c). On a fixed strain mismatch of 20%, the thickness of PVA layer is also demonstrated to control these two parameters, both of which display increasing linear relationship with the thickness (Fig. 3d).

The amplitude and wavelength can be precisely calculated at different strain mismatch. When the strain mismatch $\varepsilon$ is larger than the critical wrinkling strain $\varepsilon_c$, according to the finite-deformation buckling theory, the wrinkling structures can be expressed as:

$$W = \frac{2\pi t_f}{1+\varepsilon}\left(\frac{\overline{E_f}}{3\overline{E_s}(1+\xi)}\right)^{\frac{1}{3}} \tag{4}$$

$$A = 2t_f\left(\frac{\varepsilon-\varepsilon_c}{1+\varepsilon}\right)^{\frac{1}{2}}\left(\frac{\overline{E_f}}{3\overline{E_s}(1+\xi)}\right)^{\frac{1}{3}} \tag{5}$$

where $\xi = 5\varepsilon(1+\varepsilon)/32$, $\overline{E}_f = E_f/(1-\nu_f^2)$ and $\overline{E}_s = E_s/(1-\nu_s^2)$ represent the plane-strain modulus of thin film and substrate, respectively. $W$ is the wavelength, A is the amplitude, and $t_f$ is the thickness of thin film. The calculated wavelength and amplitude are consistent with the experimental result (Fig. 3c and d), suggesting the reliability of the preparation method and the wrinkle-based design.

To understand the effect of such tunable surface topography, laser diffraction tests were conducted on the 1.2-μm PVA sample using the setup shown in Fig. 3e with three different wavelengths (650, 532, and 450 nm). It reveals a dynamic and controllable diffraction process upon

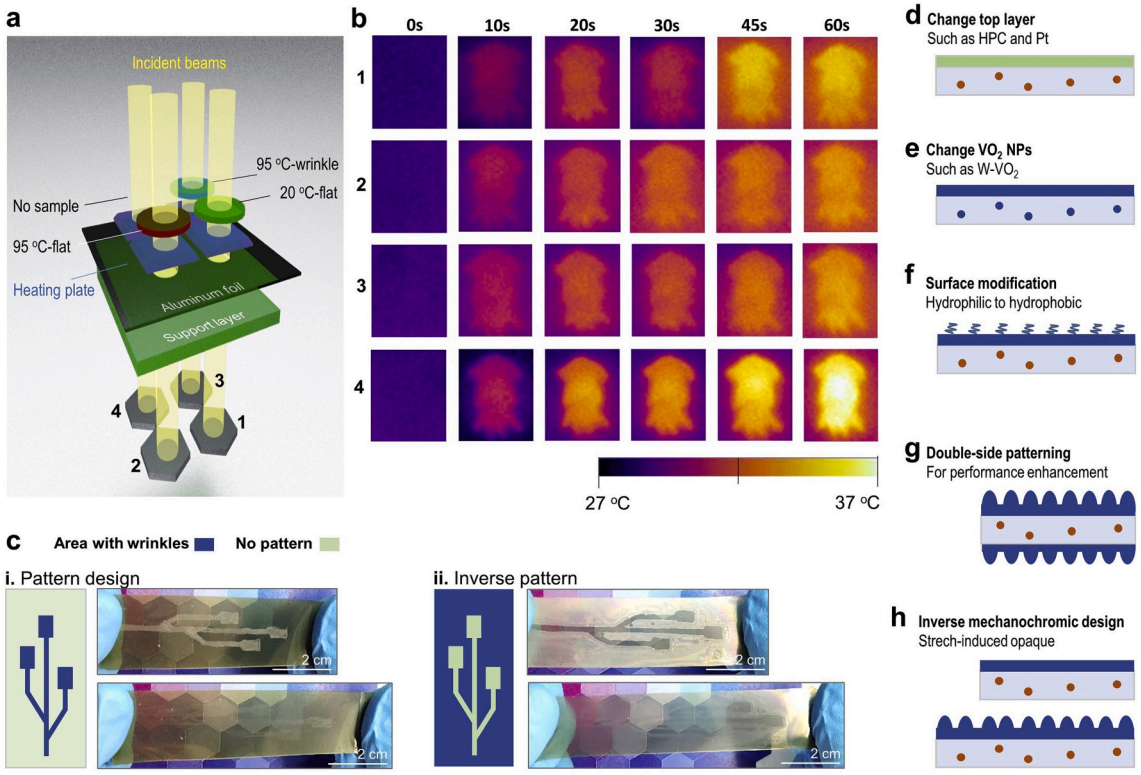


**Fig. 5.** Demo and the versatility of designs. (a) Schematic of the experimental setup for the proof-of-concept demo. Three states of the sample and a reference (empty hole) are tested as denoted in the figure. An aluminium foil is added to block the heat transfer through the solid part of the support layer. (b) Infrared camera images of the cephalopod-shaped aluminum foil on positions 1–4 as in (a). (c) Demonstration of pattern designs via coating the PVA on selective area. Patterning methods for "USB sign" and its inverse design, and the photograph of produced samples on release and stretch states. (d–h) Illustrations of extensive designs based on the thermo-mechano-chromic film, including (d) changes of the top layers or (e) dispersed NPs in PDMS matrix, (f) surface modification for tunable wettability, (g) double-side pattern design for performance enhancement, and (h) inverse mechanochromic design for transparent at release state.

different applied strains to all three lasers (Fig. 3f). All three incident beams are focused after passing through the film under 75% strain, while they form distinct periodic 1-dimensional (1D) patterns through the film under 0% strain (Fig. 3f). The diffraction is demonstrated to be dynamic, as evidenced by the gradual diffraction evolutions during a strains from 75% to 0% (Fig. 3f). Besides, the 1D patterning direction is parallel to the strain direction, which in turn is perpendicular to the parallel winkles, a characteristic feature of diffraction. To further investigate the effect, we measured the distance between the two 1st adjunct points ($2d$) (Fig. 3e). It is observed that the $d$ of three beams decrease under increasing strain, and on a certain strain, the $\theta$ is larger for beams with longer wavelength (Fig. 3g). The result can be described using the double-slit diffraction theory:

$$\frac{m\lambda}{W} = \sin\theta \approx \tan\theta = \frac{d}{h} \tag{6}$$

where $m = 1$ for 1st order diffraction, $\lambda$ is the wavelength of the incident light, and $W$ is the wrinkle wavelength. $h$ and $\theta$ are indicated in Fig. 3e. The W is calculated to be ~18–21 μm, being consistent with the experimental measurement.

### 3.4. Mechanism of thermochromics and durability

The achievement of thermochromics is attributed to the reversible crystal phase transition of $VO_2$(M/R) (Fig. 4a) [27–30]. At room temperature, $VO_2$(M) displays a distorted structure with zigzag-type V–V atomic chains and it changes to $VO_2$(R) with straight V–V chains above its critical temperature of ~65 °C, accompanied with significant physical property changes [31]. This crystal transition is identified as the crystal face variation revealed by temperature-dependent XRD analysis (Fig. 4b i). Under an increasing temperature from 20 to 100 °C, the peak at ~27.8° identified as (011)M shifts gradually to the ~27.6° as (110)R (Fig. 4b ii), and the peak at ~64.9° split into two, the (310)R and (002)R faces (Fig. 4b iii).

The crystal transition gives rise to significant optical property change. Our previous studies have proved that the NP structure of $VO_2$ can enhance the solar energy modulation by shifting the temperature-dependent transmittance contrast to the solar spectrum with dense energy, called the plasmon-enhanced solar energy modulation [15,26]. Here, the NPs are applied deliberately, and it is further revealed in the PDMS matrix, the LSPR on a $VO_2$(R) NP is able to concentrate the incident light on its surface, indicated as the strong electric fields (E-field) on the NP-matrix interface (Fig. 4c). The E-field, however, is significantly quenched at low-temperature $VO_2$(M) (Fig. 4c).

More importantly, it is demonstrated via simulation that the huge transmittance contrast is due to LSPR-induced strong absorbance on $VO_2$(R) rather than scattering effect. The absorption and scattering cross-section ($C_{abs}$ and $C_{scat}$) spectra of a single $VO_2$ (M/R) NP in PDMS matrix are calculated (Fig. 4d), clearly suggesting a significant absorbance enhancement in NIR range and only a slight scattering difference between its M and R phases. The dominated absorption of $VO_2$ NP can be also explained by the cross-section equations [32]:

$$C_{abs} = 4\pi k a^3 \mathrm{Im}\left[\frac{\varepsilon_o - \varepsilon_{om}}{\varepsilon_o - 2\varepsilon_{om}}\right] \tag{7}$$

$$C_{scat} = \frac{8\pi}{3} k^4 a^6 \left|\frac{\varepsilon - \varepsilon_{om}}{\varepsilon + 2\varepsilon_{om}}\right| \tag{8}$$

where $k = 2\pi/\lambda$, $\varepsilon_o$ is the optical dielectrics of $VO_2$, $\varepsilon_{om}$ is the optical dielectrics of PDMS, and $a$ is the diameter of the NP. As $a$ is much smaller

**Table 1**
Summary of current methods for smart windows regarding to their functionality.

| Category | Mechanism | Privacy mode | Energy-saving mode | Active privacy | Self-adaptive energy-saving | Independent energy-saving mode | Independent privacy mode | Two modes work simultaneously and independently | Ref. |
|---|---|---|---|---|---|---|---|---|---|
| Electro- | Redox reaction of metal oxide | ✓ | ✓ | ✓ | | | | | [5,8] |
| | Dynamic ion insertion | ✓ | ✓ | ✓ | | | | | [5,17, 18,38] |
| | Crystal orientation transition of liquid crystals | ✓ | \ | ✓ | | | | | [7,39] |
| | Reversible electrodeposition | ✓ | ✓ | ✓ | | | | | [19] |
| | Intramolecular charge transfer based on organic materials | ✓ | ✓ | ✓ | | | | | [40,41] |
| Thermo- | Phase-change of vanadium dioxide | | ✓ | | ✓ | ✓ | | | [2, 42–45] |
| | Phase-separation of hydrogel | ✓ | ✓ | | ✓ | | | | [46–48] |
| | Composition change of perovskite | ✓ | ✓ | | ✓ | | | | [49] |
| | Crystal orientation transition of liquid crystals | ✓ | \ | | | | | | [39] |
| Mechano- | Programmable reconfigurable structures | ✓ | ✓ | | ✓ | | | | [50] |
| | Dynamic wrinkles | ✓ | \ | ✓ | | | ✓ | | [36,37] |
| | Tunable delamination buckling | ✓ | \ | ✓ | | | | | [51,52] |
| Hybrid | Liquid crystals and vanadium dioxide | ✓ | ✓ | ✓ | ✓ | | | | [53] |
| | Vanadium dioxide in kirigami structures | ✓ | ✓ | ✓ | ✓ | | | | [26] |
| | Electrodeposition and ion insertion | ✓ | ✓ | ✓ | | | | | [54] |
| | Dynamic wrinkles and delamination | ✓ | | ✓ | | | | | [11] |
| **This work** | Bio-inspired thermo-mechanochromic films | ✓ | ✓ | ✓ | ✓ | ✓ | ✓ | ✓ | |

Notes: "\" means uncertainty. "Electro-" and "Mechano-" are considered as the active control, while "Thermo-" is considered as the "Self-adaptive/Passive" control.

than $\lambda$, $C_{abs}$ become much more dominated compared to $C_{scat}$ for both M and R cases. The negligible difference in the reflection change across the phase transition is also observed in the UV-vis-NIR spectrum (Fig. S13). The result indicates the dominating absorbance effect in thermochromic mode, which is also the main reason why the strain has a negligible effect on the theremochormic mode as mechanochromics is diffraction-dominated (Fig. 2).

Theoretical calculation also suggests the performance of integrated luminous transmittance ($T_{lum}$) (Note S1) and $\Delta T_{sol}$ is strongly linked to the NP concentration in PDMS. We calculated the transmission spectra of $VO_2$ with different filling factors (Fig. S14) using the transfer matrix method (TMM) [33]. We found an optimized $\Delta T_{sol}$ of ~29% and $T_{lum}$ of ~42% is achieved on the filling factor of 3% (Fig. 4e). Further increase the filling factor leads to decrease of both the $T_{lum}$ and $\Delta T_{sol}$, which is attributed to the strong absorbance of $VO_2$ that reduces the gross light that can be modulated. Besides, the design displays good durability, for example the 1.2-μm PVA sample shows negligible transmittance variation at 1500-nm wavelength after 60-cycling test under the stimulus of 0%-to-75% strain (Fig. 4f) or 25°C-to-95 °C temperature (Fig. 4g) changes.

### 3.5. Demo and the versatility of designs

To further characterize the optical energy modulation, the 1.2-μm PVA sample was tested in a customized setup (Fig. 5a) for its three states: 25 °C flat (75% strain), 95 °C flat (75% strain), and 95 °C winkled (0% strain). IR images of a cephalopod-like foil (Fig. S15) below the sample is measured to assess the energy modulation property. The foil is detected with similar IR temperature images below the 95 °C samples of both flat and winkled state, while displaying a stronger IR signal below the 20 °C sample (Fig. 5b). This again demonstrates that in the film, thermochromics is to control the energy and is independent to the mechanochromics. A much stronger IR signal is observed without the sample blocking (Fig. 5b), which is due to the intrinsic light blocking of the sample.

The design is easily-processible and highly flexible for modification to exhibit great potential for versatile designs. By selectively coating PVA layer, films are produced with different patterned shapes, such as an opaque "USB sign" at the release state by producing wrinkle structures on the sign area only (Fig. 5c i), or the inverse pattern design (Fig. 5c ii). Both the two shapes are observed on release states only and disappear on stretch states (Fig. 5c), and corresponding dynamic processes are presented in Video S3 and S4.

Supplementary video related to this article can be found at https://doi.org/10.1016/j.nanoen.2020.104785

Moreover, several modified designs are presented for inspiration (Fig. 5d–h), which produce additional functionality while maintaining thermo- and mechano-chromics. For example, the overcoating layer can be substituted by other organic or inorganic films (Fig. 5d), such as hydroxypropyl cellulose (HPC) (Fig. S16) or platinum (Pt) (Fig. S17). The thermochromic NPs can be substituted (Fig. 5e) for example, by the tungsten-doped $VO_2$ (W-$VO_2$) with the lower transition temperature (Figs. S18 and S19). Besides, the surface wettability is tunable (Fig. 5f) for example, by the O-plasma to be more hydrophilic or the octadecytrichlorosilane (OTS) for being more hydrophobic (Fig. S20). Also, the enhanced optical modulation is achievable (Fig. 5g), for example a double-side wrinkled film is prepared by simply coating the PVA on both sides of PDMS (Fig. S21), displaying enhanced mechanochromics than single-side design (Fig. S22). In addition, the optical modulation mode is changeable by design modification (Fig. 5h). For example, films are

successfully produced to be transparent at release state and opaque at stretch state (inverse mechanochromics to the 1.2-μm PVA sample) through coating the Pt (Fig. S23) or silicon oxide (SiOx) (Fig. S24) layers on release states of PDMS.

It is challenging to independently control the privacy and energy-saving functionalities in one window. Current methods either linked the energy-saving and privacy modes together or can fulfil one mode only (Table 1). We circumvent this issue by distinguishing their difference in spectrum range and target acceptors. To our knowledge, the concept of distinguishing and achieving the two modes has not been reported. For application, to achieve the independence of two modes is meaningful for practical window application. For example, architectural windows are to maintain\increase the indoor solar irradiation in cold days (Fig. 1c i and ii) and to decrease the irradiation in hot days to cut down the energy consumption of air condition (Fig. 1c iii and iv). Such novel bio-inspired smart window can control the privacy mode independently without influencing the favored energy-saving mode, which is not achievable by the current smart window technologies as summarized in Table 1. Such dual stimulus integrates the thermochormics which is considered as an adaptive way and desirable for energy-saving mode, with the mechanochromics which is an active control working for privacy mode (Table 1). However, futher improvement to the protype is necessary for practical use, for example, to enhance the $\Delta T_{sol}$ and reduce the transition temperature using high-crystallinity doped $VO_2$ NPs, or to lower the desirable strain for the privacy mode.

An in-depth understanding is developed for material and optical modulation. The plasmonics on $VO_2$ is related to the strong absorbance, while the scattering effect is more prominent in most of metal plasmonic materials [34,35]. The two characteristics of thermal-response and plasmonic-induced absorbance makes $VO_2$(M/R) be a unique plasmonic material and extremely suitable for this design. Besides, the wrinkle-based structure is widely reported to reduce the transmitted light in normal angle [36,37], while is proved here without jeopardizing the integrated transmitted light which is essential for energy-saving mode due to the predominated diffraction-based mechanism. Much more importantly, such a design principle of independently controlling scattering and absorbance independently can be readily applied to other smart windows, for example, to integrate the electric-controlled dynamic texture with the thermochromic materials, or to introduce transparent electronic thermal devices for active-control of the thermochromic materials.

## 4. Conclusion

In summary, we present the prototype to achieve both the on-demand privacy and adaptive energy-saving functionalities on a smart window. Inspired by the cephalopod, a thermo- and mechano-chromic film is developed to independently control the scattering for privacy and the absorbance for energy-saving modes, respectively. While maintaining a fixed solar energy modulation of ($\Delta T_{sol}$) of ~11.5%, the design can dynamically control visible transmittance ($T_{vib}$) from 60% to 17%, adding a new dimension to vanadium dioxide ($VO_2$) -based smart windows. The dynamic scattering is demonstrated due to the winkle-induced diffraction and the tunable absorbance is due to the temperature-dependent active LSPR of $VO_2$, which agrees well with the simulated and theoretical results. We further develop various designs which are highly flexible that can be modified to a series of derived designs for multi-functionality. The work may set the foundation for independent dual-mode smart windows to inspire further development in window technology, energy economization, solar energy utilization, plasmonic material, wrinkle structure, bio-inspired design, as well as fundamental investigations on dynamic optics.

## Declaration of competing interest

The authors declare no competing interests.

## CRediT authorship contribution statement

**Yujie Ke:** Conceptualization, Data curation, Formal analysis, Investigation, Methodology, Visualization, Writing - original draft, Writing - review & editing. **Qiuting Zhang:** Conceptualization, Data curation, Formal analysis, Investigation, Software, Writing - original draft, Writing - review & editing. **Tao Wang:** Data curation, Formal analysis, Investigation, Software, Writing - original draft. **Shancheng Wang:** Data curation, Methodology, Resources, Visualization. **Na Li:** Methodology, Visualization. **Gaojian Lin:** Formal analysis, Software. **Xinghai Liu:** Validation, Resources. **Zhendong Dai:** Validation, Resources. **Jing Yan:** Validation, Resources, Writing - review & editing. **Jie Yin:** Validation, Resources, Software, Writing - review & editing. **Shlomo Magdassi:** Validation, Resources, Writing - review & editing. **Dongyuan Zhao:** Validation, Resources, Writing - review & editing. **Yi Long:** Conceptualization, Formal analysis, Funding acquisition, Investigation, Project administration, Resources, Supervision, Validation, Visualization, Writing - review & editing.

## Acknowledgments

Y. Long thanks to the funding support by the National Research Foundation, Prime Minister's Office, Singapore under its Campus for Research Excellence and Technological Enterprise (CREATE) programme and Sino-Singapore International Joint Research Institute for funding support.

## Appendix A. Supplementary data

Supplementary data to this article can be found online at https://doi.org/10.1016/j.nanoen.2020.104785.

## References

[1] Y. Ke, J. Chen, G. Lin, S. Wang, Y. Zhou, J. Yin, P.S. Lee, Y. Long, Adv. Energy Mater. 9 (2019) 1902066.
[2] Y. Cui, Y. Ke, C. Liu, Z. Chen, N. Wang, L. Zhang, Y. Zhou, S. Wang, Y. Gao, Y. Long, Joule 2 (2018) 1707–1746.
[3] Y. Gao, H. Luo, Z. Zhang, L. Kang, Z. Chen, J. Du, M. Kanehira, C. Cao, Nano Energy 1 (2012) 221–246.
[4] Y. Ke, C. Zhou, Y. Zhou, S. Wang, S.H. Chan, Y. Long, Adv. Funct. Mater. 28 (2018) 1800113.
[5] G. Cai, J. Wang, P.S. Lee, Acc. Chem. Res. 49 (2016) 1469–1476.
[6] H.-N. Kim, S. Yang, Adv. Funct. Mater. 30 (2020) 1902597.
[7] H. Khandelwal, A.P.H.J. Schenning, M.G. Debije, Adv. Energy Mater. 7 (2017) 1602209.
[8] G. Cai, P. Darmawan, X. Cheng, P.S. Lee, Adv. Energy Mater. 7 (2017) 1602598.
[9] G. Cai, X. Wang, M. Cui, P. Darmawan, J. Wang, A.L.-S. Eh, P.S. Lee, Nano Energy 12 (2015) 258–267.
[10] G. Cai, X. Cheng, M. Layani, A.W.M. Tan, S. Li, A.L.-S. Eh, D. Gao, S. Magdassi, P. S. Lee, Nano Energy 49 (2018) 147–154.
[11] H.-N. Kim, D. Ge, E. Lee, S. Yang, Adv. Mater. 30 (2018) 1803847.
[12] H. Cho, J. Kwon, I. Ha, J. Jung, Y. Rho, H. Lee, S. Han, S. Hong, C.P. Grigoropoulos, S.H. Ko, Sci. Adv. 5 (2019), eaav4916.
[13] T. Chang, X. Cao, L.R. Dedon, S. Long, A. Huang, Z. Shao, N. Li, H. Luo, P. Jin, Nano Energy 44 (2018) 256–264.
[14] J. Zheng, S. Bao, P. Jin, Nano Energy 11 (2015) 136–145.
[15] Y. Ke, X. Wen, D. Zhao, R. Che, Q. Xiong, Y. Long, ACS Nano 11 (2017) 7542–7551.
[16] S. Zhang, S. Cao, T. Zhang, Q. Yao, A. Fisher, J.Y. Lee, Mater. Horiz. 5 (2018) 291–297.
[17] A. Llordés, Y. Wang, A. Fernandez-Martinez, P. Xiao, T. Lee, A. Poulain, O. Zandi, C.A. Saez Cabezas, G. Henkelman, D.J. Milliron, Nat. Mater. 15 (2016) 1267.
[18] S. Cao, S. Zhang, T. Zhang, Q. Yao, J.Y. Lee, Joule 3 (2019) 1152–1162.
[19] C.J. Barile, D.J. Slotcavage, J. Hou, M.T. Strand, T.S. Hernandez, M.D. McGehee, Joule 1 (2017) 133–145.
[20] C. Xu, G.T. Stiubianu, A.A. Gorodetsky, Science 359 (2018) 1495.
[21] E.M. Leung, M. Colorado Escobar, G.T. Stiubianu, S.R. Jim, A.L. Vyatskikh, Z. Feng, N. Garner, P. Patel, K.L. Naughton, M. Follador, E. Karshalev, M.D. Trexler, A. A. Gorodetsky, Nat. Commun. 10 (2019) 1947.
[22] Y. Bao, Y. Han, L. Yang, N. Li, J. Luo, W. Qu, R. Chen, A.K.Y. Jen, T. Li, H. Chen, W.-L. Song, D. Fang, Adv. Funct. Mater. 29 (2019) 1806383.
[23] S. Zeng, D. Zhang, W. Huang, Z. Wang, S.G. Freire, X. Yu, A.T. Smith, E.Y. Huang, H. Nguon, L. Sun, Nat. Commun. 7 (2016) 11802.
[24] Q. Guo, B. Huang, C. Lu, T. Zhou, G. Su, L. Jia, X. Zhang, Mater. Horiz. 6 (2019) 996–1004.

[25] P.A. Guerette, S. Hoon, D. Ding, S. Amini, A. Masic, V. Ravi, B. Venkatesh, J. C. Weaver, A. Miserez, ACS Nano 8 (2014) 7170–7179.
[26] Y. Ke, Y. Yin, Q. Zhang, Y. Tan, P. Hu, S. Wang, Y. Tang, Y. Zhou, X. Wen, S. Wu, T. J. White, J. Yin, J. Peng, Q. Xiong, D. Zhao, Y. Long, Joule 3 (2019) 858–871.
[27] J.D. Budai, J. Hong, M.E. Manley, E.D. Specht, C.W. Li, J.Z. Tischler, D. L. Abernathy, A.H. Said, B.M. Leu, L.A. Boatner, R.J. McQueeney, O. Delaire, Nature 515 (2014) 535–539.
[28] M. Liu, B. Su, Y.V. Kaneti, Z. Chen, Y. Tang, Y. Yuan, Y. Gao, L. Jiang, X. Jiang, A. Yu, ACS Nano 11 (2017) 407–415.
[29] Y. Ke, I. Balin, N. Wang, Q. Lu, A.I.Y. Tok, T.J. White, S. Magdassi, I. Abdulhalim, Y. Long, ACS Appl. Mater. Interfaces 8 (2016) 33112–33120.
[30] K. Liu, S. Lee, S. Yang, O. Delaire, J. Wu, Mater. Today 21 (2018) 875–896.
[31] Y. Ke, S. Wang, G. Liu, M. Li, T.J. White, Y. Long, Small 14 (2018), e1802025.
[32] L. Novotny, B. Hecht, Principles of Nano-Optics, Cambridge University Press, Cambridge, 2006.
[33] S.Y. Li, G.A. Niklasson, C.G. Granqvist, J. Appl. Phys. 108 (2010), 063525.
[34] N. Jiang, X. Zhuo, J. Wang, Chem. Rev. 118 (2018) 3054–3099.
[35] A. Agrawal, S.H. Cho, O. Zandi, S. Ghosh, R.W. Johns, D.J. Milliron, Chem. Rev. 118 (2018) 3121–3207.
[36] G. Lin, P. Chandrasekaran, C. Lv, Q. Zhang, Y. Tang, L. Han, J. Yin, ACS Appl. Mater. Interfaces 9 (2017) 26510–26517.
[37] B. Jiang, L. Liu, Z. Gao, W. Wang, Adv. Opt. Mater. 6 (2018) 1800195.
[38] S. Chen, Z. Wang, H. Ren, Y. Chen, W. Yan, C. Wang, B. Li, J. Jiang, C. Zou, Sci. Adv. 5 (2019), eaav6815.
[39] X. Liang, S. Guo, M. Chen, C. Li, Q. Wang, C. Zou, C. Zhang, L. Zhang, S. Guo, H. Yang, Mater. Horiz. 4 (2017) 878–884.
[40] D.T. Christiansen, J.R. Reynolds, Macromolecules 51 (2018) 9250–9258.
[41] Y. Wang, S. Wang, X. Wang, W. Zhang, W. Zheng, Y.-M. Zhang, S.X.-A. Zhang, Nat. Mater. 18 (2019) 1335–1342.
[42] Q. Hao, W. Li, H. Xu, J. Wang, Y. Yin, H. Wang, L. Ma, F. Ma, X. Jiang, O. G. Schmidt, P.K. Chu, Adv. Mater. 30 (2018) 1705421.
[43] T. Chang, X. Cao, N. Li, S. Long, Y. Zhu, J. Huang, H. Luo, P. Jin, Matter 1 (2019) 734–744.
[44] Y.F. Gao, S.B. Wang, L.T. Kang, Z. Chen, J. Du, X.L. Liu, H.J. Luo, M. Kanehira, Energy Environ. Sci. 5 (2012) 8234–8237.
[45] Y.F. Gao, S.B. Wang, H.J. Luo, L. Dai, C.X. Cao, Y.L. Liu, Z. Chen, M. Kanehira, Energy Environ. Sci. 5 (2012) 6104–6110.
[46] Y. Zhou, Y. Cai, X. Hu, Y. Long, J. Mater. Chem. 2 (2014) 13550.
[47] Y. Zhou, M. Layani, S. Wang, P. Hu, Y. Ke, S. Magdassi, Y. Long, Adv. Funct. Mater. 28 (2018) 1705365.
[48] X.-H. Li, C. Liu, S.-P. Feng, N.X. Fang, Joule 3 (2019) 290–302.
[49] J. Lin, M. Lai, L. Dou, C.S. Kley, H. Chen, F. Peng, J. Sun, D. Lu, S.A. Hawks, C. Xie, F. Cui, A.P. Alivisatos, D.T. Limmer, P. Yang, Nat. Mater. 17 (2018) 261–267.
[50] Y. Tang, G. Lin, S. Yang, Y.K. Yi, R.D. Kamien, J. Yin, Adv. Mater. 29 (2017) 1604262.
[51] A.V. Thomas, B.C. Andow, S. Suresh, O. Eksik, J. Yin, A.H. Dyson, N. Koratkar, Adv. Mater. 27 (2015) 3256–3265.
[52] D. Ge, E. Lee, L. Yang, Y. Cho, M. Li, D.S. Gianola, S. Yang, Adv. Mater. 27 (2015) 2489–2495.
[53] X. Liang, M. Chen, S. Guo, L. Zhang, F. Li, H. Yang, ACS Appl. Mater. Interfaces 9 (2017) 40810–40819.
[54] S.M. Islam, T.S. Hernandez, M.D. McGehee, C.J. Barile, Nat. Energy 4 (2019) 223–229.

Yujie Ke is currently a research fellow in Dr. Yi Long group, Nanyang Technological University, Singapore. He got his Ph.D. degree from the same instituie in 2019. He obtained his B.E and Master degrees from Wuhan Institute of Technology, China in 2013 and University at Buffalo, the State University of New York (SUNY-Buffalo), US in 2015, respectively. His research interest includes vanadium dioxide, mechano-/thermochromism, stimulus-responsive and plasmonic materials, energy-efficient smart windows.

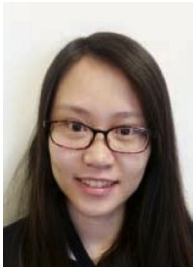

Qiuting Zhang is currently a postdoctoral fellow in Yale University, USA. She graduated from Beijing Institute of Technology with a B.E. degree in 2014 and received her Ph.D. degree from Temple University in Mechanical Engineering in 2019. She loves solving hard mechanical problems and also searching for good food in the city. Her research interests include mechanics and functionality of extreme mechanical instabilities.

Tao Wang joined Soochow University as a full professor in 2019. He received his Ph.D. degree in Physics from University of Paris-Sud (Paris 11) in 2012. After that, he then worked at RWTH Aachen University, Germany from 2012 to 2014, at National University of Singapore from 2014 to 2017, and as a Research Scientist at Institute of Materials Research and Engineering (IMRE), A*STAR, Singapore from 2017 to 2019. He is interested in plasmon-based electrically-driven nano light sources.

Shancheng Wang obtained his BEng (Hons) in 2016 from Nanyang Technological University (NTU), Singapore. He is currently a PhD student in the School of Material Science and Engineering of NTU. His research specializes in functional thin films, and he is focusing on the development of vanadium oxides for thermochromic smart coatings.

Na Li is currently a visiting student in Dr. Yi Long's team in the School of Material Science and Engineering at Nanyang Technological University, Singapore. She is a Ph.D. candidate in Northeast Petroleum University, China. Her current research is focused on expanding the application of functional nanomaterials combing with polymers by designing different new structures.

Gaojian Lin joined Beijing Institute of Technology as an assistant professor in 2018. He obtained his B.E. degrees from university of science and technology of China (USTC) in 2014 and his Ph.D from Temple University, USA, in 2018. He is interested in mechanics and functionality of instability driven reconfigurable soft materials.

Prof. Xinghai Liu is currently the associate chair in school of printing and packing, Wuhan university, China. He obtained his Ph.D. degree in Chemistry from the same university. His research interests include intelligent packing materials as well as UV-curable resins and inks.

Zhendong Dai is a full professor and the director in the Institute of Bio-Inspired Structure and Surface Engineering in College of Mechanical and Electrical Engineering, Nanjing University of Aeronautics and Astronautics, China. His research interests include mechanical theory and design for biomimetic robotics and materials, aeronautic and astronautic technologies, and material chemistry and physics.

Jing Yan is currently an Assistant Professor of Molecular, Cellular and Developmental Biology and a member of the Quantitative Biology Institute (Qbio) at Yale University, USA. Before that, He was working at Princeton university as a joint postdoctoral researcher in the department of Molecular Biology and Mechanical and Aerospace Engineering. He obtained his B. S. and Ph.D. degree from Peking University, China and University of Illinois at Urbana-Champaign, USA, respectively.

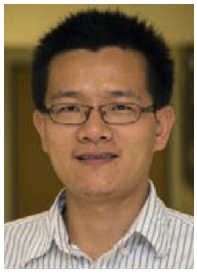

Jie Yin is currently an Assistant Professor in the Department of Mechanical and Aerospace Engineering, North Carolina State University, Raleigh, NC, USA. He worked as an Associate Professor at Temple University and Postdoctoral Associate at Massachusetts Institute of Technology. He obtained his Ph.D. degree from Columbia University and M.S. from Tsinghua University. His research focuses on multifunctional interfacial materials for energy saving and water harvesting, mechanical metamaterials, and soft robotics.

Shlomo Magdassi is a professor at the Institute of Chemistry, the Hebrew University of Jerusalem, Israel. His research focuses on the formation, formulation and applications of micro and nanoparticles in various fields including 2D, 3D and 4D printing. The results of some of his research led to industrial activities such as worldwide sales and establishment of new companies. Currently he is the Head of the Institute of Chemistry, and of the Functional and 3D Printing Center at The Hebrew University.

Dongyuan Zhao is now the director of the Laboratory of Advanced Materials at Fudan University (China). He is also the Co-Director of the 2011 Collaborative Innovation Center of Chemistry for Energy Materials (iChEM). He received his B.S. (1984) and Ph.D. (1990) from Jilin University. He was elected as an academician of the Chinese Academy of Science in 2007, and a member of The World Academy of Science (TWAS) in 2010. His research interests are focused on the interfacial assembly and macroscopic control of ordered mesoporous materials for applications in catalysis, energy, water purification and biomedicine.

Yi Long is a Senior Lecturer in the School of Materials Science and Engineering, Nanyang Technological University. She obtained her Ph.D. degree from the University of Cambridge, UK. She has successfully implemented technology transfer from lab to industry for hard-disk company in her early career life. Her recent research is to develop micro/nanostructured functional materials and devices with focus on energy-saving smart windows and flexible/stretchable electronics.